tvst

Cornea & External Disease

Characterization of Directional Reflectance in Corneal Tissue: A Comprehensive Optical Coherence Tomography Analysis

Jad F. Assaf[1], Jiachi Hong[1], Yan Li[1], and David Huang[1]

[1] Casey Eye Institute, Oregon Health & Science University, Portland, OR, USA

Correspondence: David Huang, Casey Eye Institute, Oregon Health & Science University, Portland, USA. e-mail: huangd@ohsu.edu

Received: October 15, 2024
Accepted: February 24, 2025
Published: April 3, 2025

Keywords: corneal reflectance; optical coherence tomography (OCT); corneal microstructure; directional reflectance; incidence angle

Citation: Assaf JF, Hong J, Li Y, Huang D. Characterization of directional reflectance in corneal tissue: A comprehensive optical coherence tomography analysis. Transl Vis Sci Technol. 2025;14(4):7, https://doi.org/10.1167/tvst.14.4.7

Purpose: To characterize the directional reflectance properties of the cornea using optical coherence tomography (OCT) imaging and develop a mathematical model describing corneal reflectance as a function of depth and incidence angle across different corneal layers.

Methods: A retrospective analysis was conducted on OCT scans from normal subjects using the Visionix Avanti OCT system (840 nm). Reflectance values for the epithelium, Bowman's layer, stroma, and endothelium/Descemet's membrane were extracted and analyzed as functions of incidence angle and corneal depth. Reflectance distributions were assessed for normality. Exponential functions were fitted to the mean and 97th percentile reflectance data to model directional reflectance for each corneal layer.

Results: Reflectance values exhibited non-normal leptokurtic distributions with right-tailed skewness, requiring non-parametric methods for percentile calculations. The exponential model incorporating angular dependence achieved R^2 values of 0.987 and 0.963 for mean and 97th percentile reflectance, respectively. The mean reflectance of the epithelium was modeled by a single exponential function, with half-reflectance angles of 15.9° to 26.6°. The stromal layers required two exponential components, with the anterior stroma exhibiting the highest reflectance and most pronounced directionality (half-reflectance angle of 0.17°). The 97th percentile reflectance differed, with higher reflectance values in the middle and posterior stroma. No statistically significant age or gender related variability in reflectance was measured.

Conclusions: This study provides a detailed mathematical model of corneal directional reflectance, highlighting the importance of incidence angle and layer depth in OCT image analysis.

Translational Relevance: The developed cornea reflectance model may improve OCT-based diagnostics by identifying early microstructural changes, aiding in the diagnosis and management of corneal diseases.

Introduction

The cornea, a transparent, avascular tissue forming the anterior part of the eye, is fundamental in refracting and transmitting light onto the retina, thus playing a critical role in visual acuity.[1] Composed primarily of organized collagen fibers and interspersed cellular elements, its structural integrity is essential for maintaining its optical clarity and function.[2]

Optical coherence tomography (OCT) has emerged as a powerful, non-invasive imaging modality in ophthalmology, providing high-resolution, cross-sectional images of ocular structures, including detailed views of corneal layers.[3,4] Beyond morphological assessment, OCT allows for the analysis of tissue optical properties through reflectance measurements. These reflectance profiles can offer valuable insights into tissue microstructure, scattering properties, and potential pathological alterations.[5]

Previous seminal studies by Knighton et al.[6,7] extensively characterized the directional reflectance properties of the retina, revealing significant relationships between retinal microstructure and reflectance

patterns. These works highlighted how variations in tissue composition and organization influence light scattering and reflectance. Despite the cornea's importance, similar comprehensive analyses of its directional reflectance properties are lacking.

The cornea is susceptible to various pathologies such as keratoconus, corneal dystrophies, and scarring, which can disrupt its microarchitecture and alter its optical properties.[8,9] Understanding the directional reflectance of the cornea could enhance the diagnostic capabilities of OCT by providing additional quantitative metrics related to corneal health and integrity. Such metrics could aid in the early detection of corneal pathologies, monitoring disease progression, and evaluating treatment outcomes, potentially informing novel diagnostic and therapeutic strategies.

Therefore this study aims to characterize the directional reflectance of the cornea using OCT imaging. By analyzing reflectance across segmented corneal layers—the epithelium, stroma, and endothelium—and modeling reflectance as a function of layer depth and angle of incidence, we seek to develop a comprehensive model describing the cornea's reflectance characteristics. By bridging gaps in current understanding and exploring the corneal structure-function relationship, this study sets the stage for future investigations into the complex interplay between corneal structure and optical behavior.

Methods

This retrospective study was conducted at the Casey Eye Institute of Oregon Health & Science University (OHSU) and received approval from the OHSU Institutional Review Board. All procedures adhered to the tenets of the Declaration of Helsinki and complied with the Health Insurance Portability and Accountability Act of 1996. Patient data were anonymized to protect confidentiality.

Patient Selection

We analyzed OCT scans from a cohort of normal subjects to evaluate corneal reflectance properties. Informed consent was obtained from all subjects after a detailed explanation of the study's nature, procedures, and potential consequences. Inclusion criteria encompassed patients with 6-mm-wide OCT scans obtained using the Visionix (formerly Optovue) Avanti platform (North Lombard, IL, USA). Subjects were classified as normal or pre-LASIK candidates based on comprehensive ophthalmic examinations, including slit-lamp biomicroscopy, ensuring the absence of corneal abnormalities. Exclusion criteria included any history of corneal pathology, prior refractive surgery, or any ocular condition that could affect corneal reflectance.

OCT Imaging and Calibration

All OCT scans were performed using the Avanti OCT system, operating at a wavelength of 840 nm with an axial resolution of approximately 5 µm. To ensure accurate reflectivity measurements, the OCT device underwent a rigorous calibration process. We utilized near-Lambertian diffuse reflectance targets (Spectralon, North Sutton, NH, USA) with known reflectance rates of 12%, 25%, and 50% to map the squared magnitude of the OCT signal to absolute reflectance values. A linear regression analysis was performed to establish the relationship between the OCT signal and the known reflectance standards, allowing for the estimation of the magnitude corresponding to 100% reflectance. The 99% reflectance panel was omitted from direct measurements to prevent detector saturation. Additionally, the reflectors' angle dependence was minimal, with less than ±4% variation in reflectance observed over a 25° range of incidence angles.

After calibration, OCT signal intensities were converted to absolute reflectance values by normalizing against the calculated 100% reflectance magnitude. This standardization facilitates consistent data analysis across different OCT devices and imaging sessions.

Data Acquisition and Preparation

For each subject, eight non-dewarped radial B-scan images were extracted from the OCT data. The non-dewarped images preserve the true optical representation of the cornea, ensuring that each A-scan corresponds accurately to the physical path of the OCT beam through the cornea. Pixel intensities in these images represent the reflectance of the tissue in the linear domain.

To correct for the inherent depth-dependent sensitivity loss and to mitigate speckle noise, we applied a depth-dependent signal roll-off compensation[10]—derived from calibration with a diffuse reflectance target—followed by a low-pass mean filter.[11] This processing pipeline rectifies the intensity data to yield accurate reflectance estimates that are generalizable to other devices.

Incidence Angle Calculation

Accurate determination of the angle of incidence for each A-scan was essential for modeling directional reflectance. We leveraged the OCT system's ability to

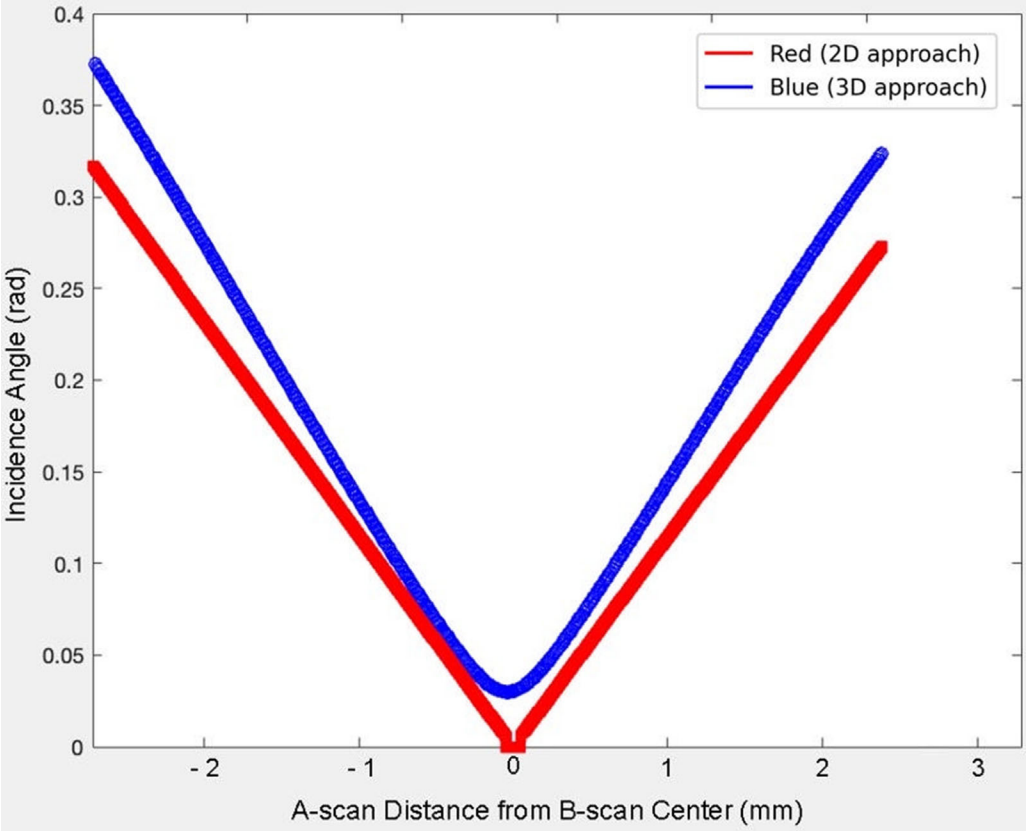

Figure 1. Comparison of incidence angle calculations using a 2D (*red*) versus 3D (*blue*) approach on an in vivo OCT B-scan of a normal cornea. The X-axis represents the lateral positions of the A-scans, and the Y-axis shows the corresponding incidence angles in radians. In this example, the B-scan does not pass directly through the corneal apex, so the 3D incidence angle (*blue*) never reaches zero. The 3D approach also accounts for out-of-plane incidence angles, leading to consistently larger values than the 2D calculation.

image the curved cornea in vivo, which inherently provides a range of incidence angles because of the curvature of the cornea relative to the OCT beam. By assuming that the cornea is homogeneous at the same depths across the central and paracentral areas, we could utilize data from different regions to analyze reflectance at varying incidence angles without physically manipulating the light source or detector.

We used a three-dimensional (3D) approach with corneal surface elevation data used to compute surface normals at each point on the anterior corneal surface. The incidence angle (θ) was calculated as the angle between the OCT beam vector in air and the normal vector to the corneal surface at each A-scan location.

This 3D method accounts for both in-plane and out-of-plane curvatures of the cornea, providing a more precise calculation of incidence angles compared to a two-dimensional (2D) method, which assumes that the B-scan intersects the corneal apex and neglect out-of-plane variations. Figure 1 illustrates the differences between 2D and 3D incidence angle calculations on a sample OCT B-scan.

Corneal Layer Segmentation

The cornea was segmented into the epithelium, Bowman's layer, stroma, and endothelium/Descemet's membrane for analysis. The epithelium's posterior boundary was defined using the Avanti system's automated algorithm. Bowman's layer was defined as the 10 µm region just posterior to the epithelium, measured perpendicular to the local corneal tangent. The stroma, spanning from Bowman's layer to the endothelium, was further divided into anterior, middle, and posterior thirds. The endothelium and Descemet's membrane comprised the innermost 15 µm of the cornea. The anterior 25% of the epithelium was excluded from analysis due to the high reflectance from the air-tear interface. The variability of the tear film can affect the underlying anterior epithelial reflectance, and the limited axial resolution of the OCT system—defined by its point spread function—causes the strong reflectance from the air-tear interface to overlap with and obscure the reflectance from the underlying anterior epithelium.

Superpixel Creation and Binning

To analyze reflectance properties systematically, each pixel in the OCT images was first associated with two parameters: corneal depth and the incidence angle. We then divided the images into superpixels by grouping pixels that fell within narrow, predefined ranges: 2% increments in corneal depth and 0.001 radians in incidence angle. This grouping effectively clusters the data into regions with nearly identical depth and angular characteristics, ensuring that the aggregated reflectance values accurately represent the optical behavior for that specific region of the cornea.

Superpixels with similar parameters (depth and incidence angles) across all subjects in the dataset were then grouped together into bins. This binning strategy allowed us to aggregate sufficient data for mean reflectance analysis, which provides insight into the average reflectance changes across the cornea, capturing the overall optical behavior of each layer. Additionally, the 97th percentile reflectance within each bin was assessed, reflecting higher-intensity scattering events that may indicate corneal opacities or subtle structural variations. The choice of a 2% depth increment and a 0.001 radian bin width was determined empirically to balance depth and angular resolution with the requirement for sufficient data in each bin.

Reflectance Normality Testing

Before further analysis, we assessed the normality of reflectance values within each bin to determine the appropriate statistical methods for percentile extraction. Normality testing helps decide whether standard deviation can be used for extracting percentiles or if non-parametric approaches are necessary.

We performed normality testing for the reflectance of all pixels in the individual corneal layers—epithelium, stroma, and endothelium—before further analyzing superpixel bins. The D'Agostino-Pearson omnibus K-squared test was used, with a significance level (α) of 0.05. Layers or bins with P values >0.05 were considered to have normally distributed reflectance values, whereas those with P values ≤ 0.05 were deemed non-normal.

The proportion of bins that passed or failed the normality test was recorded. We also visualized their distribution across the cornea to determine whether normality patterns were associated with specific corneal regions or layers.

Curve Fitting and Reflectance Modeling

We modeled the mean and 97th percentile reflectance profiles as functions of the incidence angle for all superpixel bins across the entire cornea. Inspired by Knighton et al.[7]—who used an exponential function to describe directional reflectance in the retinal nerve fiber layer—we adopted a similar approach but allowed up to three exponential components to accommodate the more complex reflectance behavior in corneal layers.

To determine the appropriate number of components, we first fitted a single-exponential model. If $R^2 > 0.90$, it was considered sufficient unless adding another component reduced $\geq 50\%$ of the remaining gap toward a perfect fit ($R^2 = 1.0$). This strategy ensured that additional complexity was only introduced when it provided meaningful improvement, thereby preventing overfitting. Moreover, this curve fitting approach enables extrapolation to angles of incidence not directly represented in our dataset, including large angles or near-zero angles subject to flare artifacts.

Afterward, we grouped the results according to the predefined corneal layer segmentation (middle epithelium, posterior epithelium, Bowman's layer, anterior stroma, middle stroma, posterior stroma, and endothelium/Descemet's membrane) for analysis and presentation.

The general form of the exponential function used is:

$$I_k(\theta) = A_{1k}e^{(-B_1\theta)} + A_{2k}e^{(-B_2\theta)} + A_{3k}e^{(-B_3\theta)} + C$$

Where:

- $I_k(\theta)$ is the reflectance intensity at layer k for incidence angle θ.
- A_{1k}, A_{2k}, and A_{3k} are amplitude coefficients representing the maximum reflectance magnitudes for the first, second, and third exponential components in layer k.
- B_{1k}, B_{2k}, and B_{3k} are decay constants describing how reflectance decreases with increasing incidence angle. The decay angle is the inverse of the decay constant B, expressed as $1/B$.
- C is a constant accounting for baseline reflectance.

Curve fitting was performed using non-linear least squares optimization in MATLAB R2023b (MathWorks Inc., Natick, MA, USA). Constraints were applied to ensure physically meaningful parameters:

1. $A_{1k} > A_{2k} > A_{3k} > 0$. The amplitude coefficients were constrained to ensure each subsequent component contributes less reflectance.
2. $B_{1k}, B_{2k}, B_{3k} \leq 0$. Decay constants were constrained to be negative or zero, reflecting decreasing reflectance with increasing angle.
3. $C \geq 0$. The constant C was constrained to be non-negative, capturing the baseline reflectance.

Initial parameter estimates were based on preceding layers to promote continuity between layers. Regularization techniques were applied to penalize large parameter variations between adjacent depth layers, ensuring smooth transitions in the model. The goodness of fit was evaluated using the coefficient of determination (R^2), with values closer to 1 indicating a better fit.

Mean Variance Analysis

To quantify patient-level variability in corneal reflectance relative to our model, we performed a variance component analysis on the superpixel mean reflectance values. For each corneal layer, the residuals were computed as the percentage deviation between the measured mean reflectance of each superpixel and the model-predicted mean reflectance (linear domain). These normalized residuals were then partitioned into three variance components—between-patient, between-eye (within a patient), and within-eye—using standard one-way analysis of variance.

In addition, we investigated potential demographic influences on reflectance variability. Pearson correlation analysis was performed to assess the association between patient age and the mean of residual variance for each layer. Furthermore, to evaluate gender differences, we compared the resulting distributions between male and female subjects using a two-sample *t*-test.

Results

Subject Demographics

A total of 160 OCT scans from 95 eyes of 49 patients were analyzed. The mean age of the subjects was 38.3 ± 11.3 years (range 18–76 years), with 50% being male.

Data Distribution and Normality

Reflectance values for the epithelium, stroma, and endothelium exhibited non-normal leptokurtic distributions with a right-tailed skew ($P < 0.0001$). Specifically, 96.0% of superpixel bins in the epithelium (n = 10,200), 98.2% in the stroma (n = 51,000), and 74.3% in the endothelium (n = 4080) were non-normally distributed according to the D'Agostino-Pearson omnibus K-squared test. Approximately 3.6% of superpixel bins were found to be normally distributed, primarily at higher incidence angles where sample sizes are smaller and data are more susceptible to artifacts.

Reflectance Modeling and Curve Fitting

The mean and 97th percentile reflectance models for each corneal layer were successfully fitted using exponential functions, demonstrating high goodness of fit with average R^2 values of 0.987 for mean reflectance and 0.963 for the 97th percentile reflectance. The detailed parameters of the reflectance models for each corneal layer are presented in Tables 1 and 2.

Table 1. Mean Directional Reflectance Components of Corneal Layers

Corneal Layer	First Reflectance Coefficient A_1 (Absolute Reflectance)	First Angle of Decay ($1/B_1$)	% Reflectance of First Directional Reflectance Component	Second Reflectance Coefficient A_2 (Absolute Reflectance)	Second Angle of Decay ($1/B_2$)	% Reflectance of Second Directional Reflectance Component	Half Reflectance Angle	R^2
Middle epithelium	5.44E-14	38.5°	100	0	0°	0	26.6°	0.974
Posterior epithelium	4.30E-14	22.7°	100	0	0°	0	15.9°	0.982
Bowman's membrane	2.49E-13	2.40°	32.3	1.08E-13	11.6°	67.7	2.42°	0.982
Anterior stroma	5.52E-13	0.191°	10.2	1.08E-13	8.62°	89.8	0.172°	0.994
Middle stroma	1.90E-13	1.24°	28.4	8.64E-14	6.85°	71.6	1.29°	0.982
Posterior stroma	6.72E-13	1.15°	62.6	6.91E-14	6.67°	37.4	0.886°	0.995
Descemet's & endothelium	2.13E-12	0.814°	71.9	7.95E-14	8.55°	28.1	0.591°	0.997

The percent reflectance of the directional reflectance component is the area under the curve of each exponential component divided by the sum area-under-the-curve of all exponential components, computed from incidence angles 1° to 23°.

Table 2. Directional Reflectance Components of Corneal Layers at the 97th Percentile

Corneal Layer	First Reflectance Coefficient A_1 (Absolute Reflectance)	First Angle of Decay ($^1/_{B_1}$)	% Reflectance of First Directional Reflectance Component	Second Reflectance Coefficient A_2 (Absolute Reflectance)	Second Angle of Decay ($^1/_{B_2}$)	% Reflectance of Second Directional Reflectance Component	Third Reflectance Coefficient A_3 (Absolute Reflectance)	Third Angle of Decay ($^1/_{B_3}$)	% Reflectance of Second Directional Reflectance Component	Half Reflectance Angle	R^2
Middle epithelium	6.75E-13	1.33°	100	0	0°	0	0	0°	0	0.924°	0.943
Posterior epithelium	6.75E-13	1.89°	100	0	0°	0	0	0°	0	1.31°	0.965
Bowman's membrane	4.50E-10	0.101°	82.4	1.98E-12	2.00°	7.22	4.50E-13	12.6°	10.3	0.0702°	0.994
Anterior stroma	5.15E-11	0.191°	61.7	9.00E-13	1.67°	9.44	4.50E-13	10.2°	28.9	0.137°	0.969
Middle stroma	9.57E-09	0.157°	99.7	9.00E-13	4.88°	0.289	2.25E-13	4.84E-04°	7.20E-06	0.109°	0.972
Posterior stroma	5.86E-09	0.177°	99.5	1.85E-12	2.71°	0.480	2.58E-13	4.84E-04°	1.20E-05	0.123°	0.973
Descemet's & endothelium	3.82E-09	0.191°	98.8	4.50E-12	1.41°	0.862	3.02E-13	9.00°	0.367	0.133°	0.927

Mean Reflectance Profiles

The mean reflectance of the epithelium was modeled by a single exponential function:

$$I(\theta) = A_{\text{epi}} e^{(-Bepi\theta)}$$

This indicates a less directional reflectance pattern compared to deeper corneal layers. The half-reflectance angles (the angle at which reflectance drops to half its maximum value) for the middle and posterior epithelium were approximately 26.58° and 15.85° (Table 1), respectively, suggesting moderate angular dependence.

The stromal layers exhibited more complex mean reflectance patterns, requiring two exponential components for modeling:

$$I(\theta) = A_1 e^{(-B_1\theta)} + A_2 e^{(-B_2\theta)}$$

- Anterior Stroma: Demonstrated high reflectance and pronounced directionality, with the first (larger) component accounting for 10.2% of reflectance with a half-reflectance angle of 0.17°, indicating a sharp decrease in reflectance with increasing angle of incidence.
- Middle Stroma: Showed lower overall reflectance, with the first component contributing 28.4% of reflectance and a half-reflectance angle of 1.29°.
- Posterior Stroma: Exhibited high reflectance similar to the anterior stroma but with slightly less directionality (smaller angle of decay $^1/_{B_1}$).

The Bowman's membrane, endothelium, and Descemet's membrane also required a two-component exponential model, reflecting their unique structural composition.

Figures 2 and 3 illustrate the mean absolute reflectance as a function of corneal depth and incidence angle, respectively. The anterior and posterior stroma displayed higher reflectance compared to the middle stroma across most incidence angles.

The 97th Percentile Reflectance Profiles

The 97th percentile reflectance models and their detailed parameters are presented in Table 2. The 97th percentile reflectance profile of the epithelium was modeled as a single exponential function with a baseline constant C:

$$I(\theta) = A_{\text{epi}} e^{(-Bepi\theta)} + C$$

The Bowman's membrane, stroma, endothelium, and Descemet's membrane were modeled using three exponentials:

$$I(\theta) = A_1 e^{(-B_1\theta)} + A_2 e^{(-B_2\theta)} + A_3 e^{(-B_3\theta)} + C$$

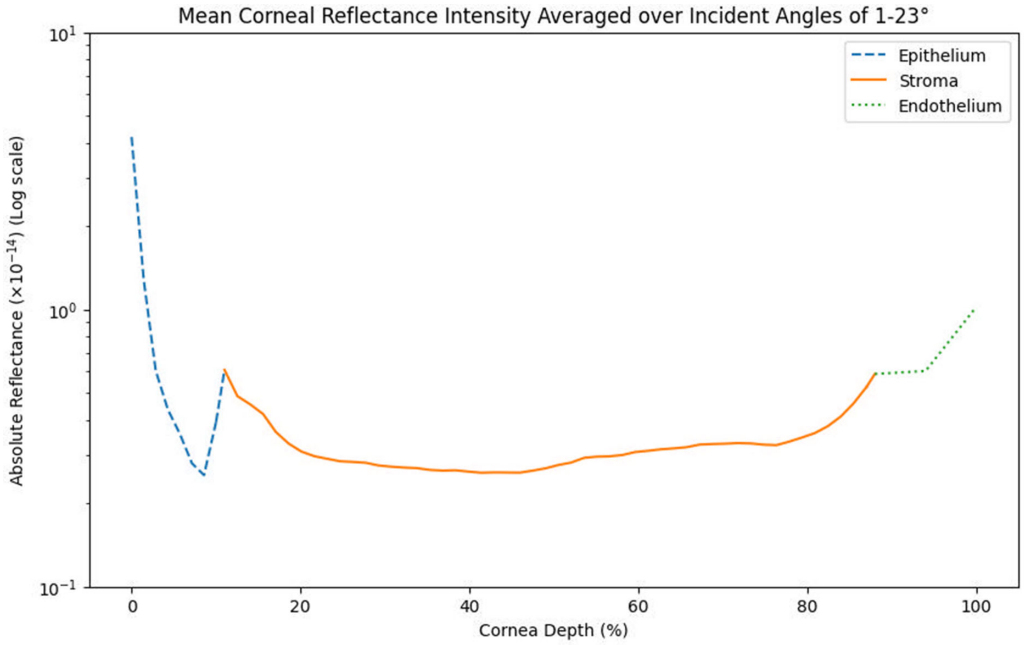

Figure 2. Absolute mean reflectance versus corneal depth, averaged over incidence angles from 1° to 23°.

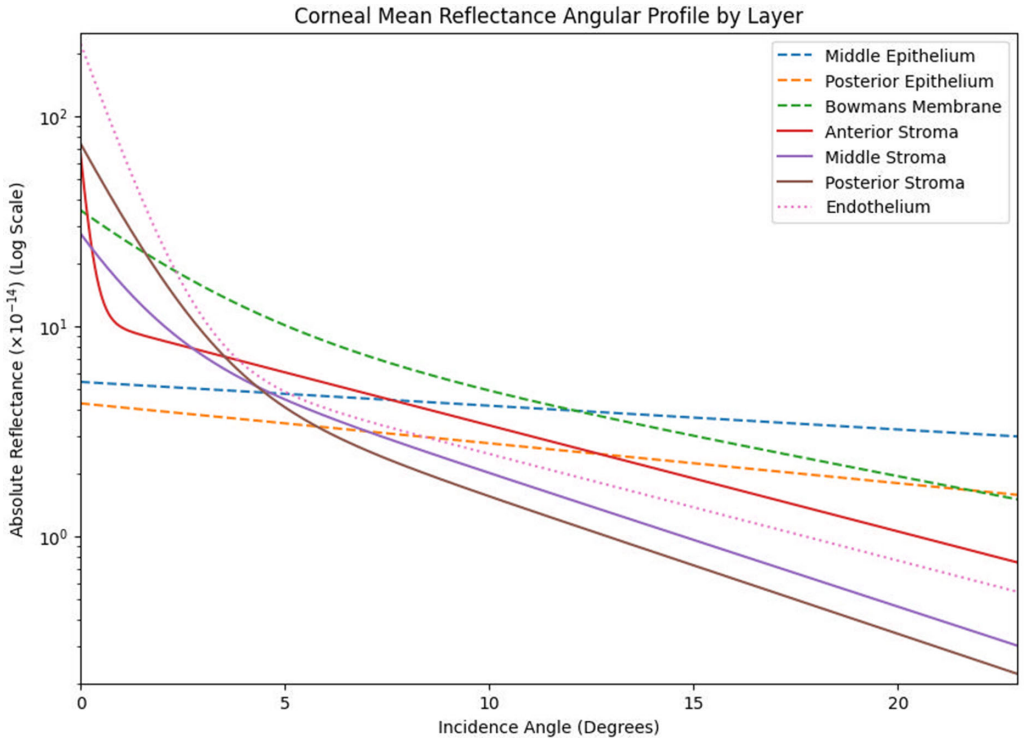

Figure 3. Absolute mean reflectance as a function of incidence angle for different corneal layers.

At the 97th percentile, reflectance models (Figs. 4, 5) showed similar patterns to mean reflectance, but the middle and posterior stroma possess higher reflectance compared to the anterior stroma.

Mean Variance Analysis

Variance component analysis of the superpixel-level residuals revealed that, in the epithelium, 31.4% of the total normalized variance (overall variance =

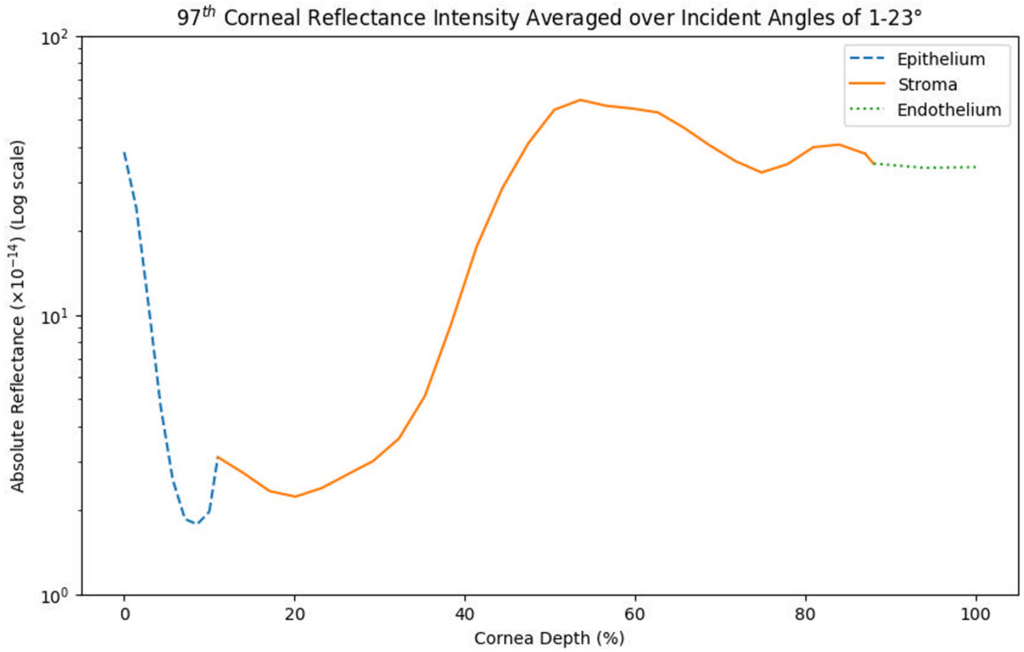

Figure 4. The 97th percentile absolute reflectance versus corneal depth, averaged over incidence angles from 1° to 23°.

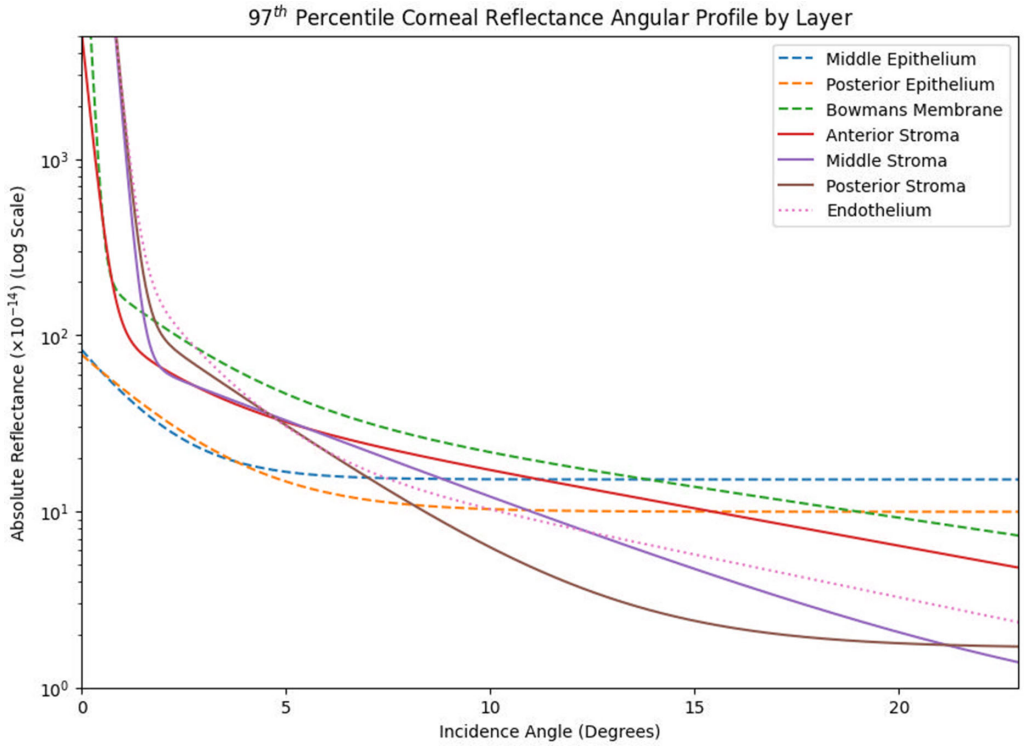

Figure 5. The 97th percentile absolute reflectance as a function of incidence angle for different corneal layers.

0.42) was attributable to differences between patients, 6.3% to differences between eyes, and 62.3% to within-eye variability. In the stroma, the variance was partitioned as 26.2% between-patient, 4.4% between-eye, and 69.5% within-eye (overall variance = 0.56). For the endothelium, the components were 38.8% between-patient, 10.5% between-eye, and 50.7% within-eye (overall variance = 0.49).

Pearson correlation analysis between patient age and normalized residual variance did not reveal any

significant associations. For the epithelium, the correlation coefficient was $r = -0.002$ ($P = 0.992$); for the stroma, $r = -0.065$ ($P = 0.667$); and for the endothelium, $r = -0.058$ ($P = 0.700$). Additionally, gender does not significantly affect corneal reflectance variability in the epithelium ($P = 0.523$), stroma ($P = 0.176$), and endothelium ($P = 0.177$).

Discussion

This study provides a comprehensive analysis of the directional reflectance properties of the cornea using OCT imaging. By modeling reflectance as a function of incidence angle and corneal depth, we developed detailed exponential models for both mean and 97th percentile reflectance profiles across different corneal layers. Our findings reveal distinct reflectance patterns and directionalities within these layers.

Reflectance values in the epithelium, stroma, and endothelium exhibited non-normal leptokurtic distributions with a right-tailed skew, necessitating the use of nonparametric techniques for percentile calculations. Approximately 3.6% of superpixel bins were normally distributed, likely because of statistical anomalies from the large number of bins tested. Most of these superpixels were at higher incidence angles where sample sizes are lower and data are subject to artifacts. At high incidence angles, the signal-to-noise ratio decreases, causing noise to overcome the signal and potentially leading to a more normal distribution.

Our results showed that the angular dependence of the mean reflectance of the middle and posterior epithelium is modeled by a single exponential function, indicating a less directional reflectance pattern. The half-reflectance angles were relatively large (26.58° and 15.85°), suggesting that reflectance decreases gradually with increasing incidence angle. This observation aligns with Rayleigh and Mie scattering theories, where small, randomly arranged scattering elements cause diffuse scattering with minimal dependence on the angle of incidence.[12,13] The epithelial cells and subcellular structures are comparable in size to the OCT wavelength (840 nm), resulting in uniform reflectance across varying angles.

In contrast, the stromal layers required two exponential components to model their mean reflectance, indicating the presence of multiple structural components, each with distinct angular dependence. The anterior and posterior stroma exhibited higher reflectance and more pronounced directionality compared to the middle stroma (Table 1; Figs. 2 and 3). The anterior stroma, with a half-reflectance angle of 0.17°, displayed the sharpest decrease in reflectance with increasing angle, indicating strong directionality. In comparison, the posterior and middle stroma had larger half-reflectance angles of 0.89° and 1.29°, respectively, reflecting a more gradual decline in reflectance and less pronounced directionality (Table 1). However, the anterior stroma exhibited a less pronounced decrease in reflectance at lower incidence angles, indicating a flatter, less directional component compared to the middle and posterior stroma (Fig. 3).

Two key structural factors that contribute to corneal transparency are the uniformity of collagen fibril diameters and the tight regulation of spacing between adjacent fibrils.[2] Our findings suggest differences in collagen fiber organization, lamellar spacing, and keratocyte density across the stromal depth.[14,15] Additionally, variations in tissue composition, such as the presence of a nerve plexus, may further contribute to these reflectance differences.[16,17] According to Ruberti et al. (2011), the organization of the corneal lamellae displays a narrowed weaving pattern in the anterior stroma, whereas in the posterior stroma, the organization transitions to a plane pattern with lamellae lying regularly in the plane of the cornea.[14] The intensity of reflectance is affected by refractive index variations within the tissue. Denser lamellae in the anterior stroma create more abrupt changes in refractive index, which can enhance reflectance intensity. The spacing between lamellae also influences reflectance; tightly packed lamellae can cause constructive interference of backscattered light, increasing reflectance, whereas regular spacing can promote destructive interference, contributing to corneal transparency.[2] Differences in lamellar density, regularity, and spacing between stromal layers may explain why the middle stroma mean reflectance is less pronounced compared to the anterior and posterior stroma.

An interesting observation in our study is the distinct patterns of magnitude and directionality between the mean and 97th percentile reflectance profiles. While the anterior and posterior stroma exhibited the highest mean reflectance, the 97th percentile reflectance was much higher in the middle and posterior stroma (Figs. 4 and 5). Despite this, the less directional component of the anterior stroma at higher incidence angles, observed in the mean reflectance, remains present relative to the middle and posterior stroma in the 97th percentile profiles as well. Different reasons may explain such discrepancy such as differences in collagen organization within the stromal layers. The anterior stroma is known to have densely packed[18] and randomly directed[19] interwoven collagen fibers.[20] In contrast, the posterior stroma has a more

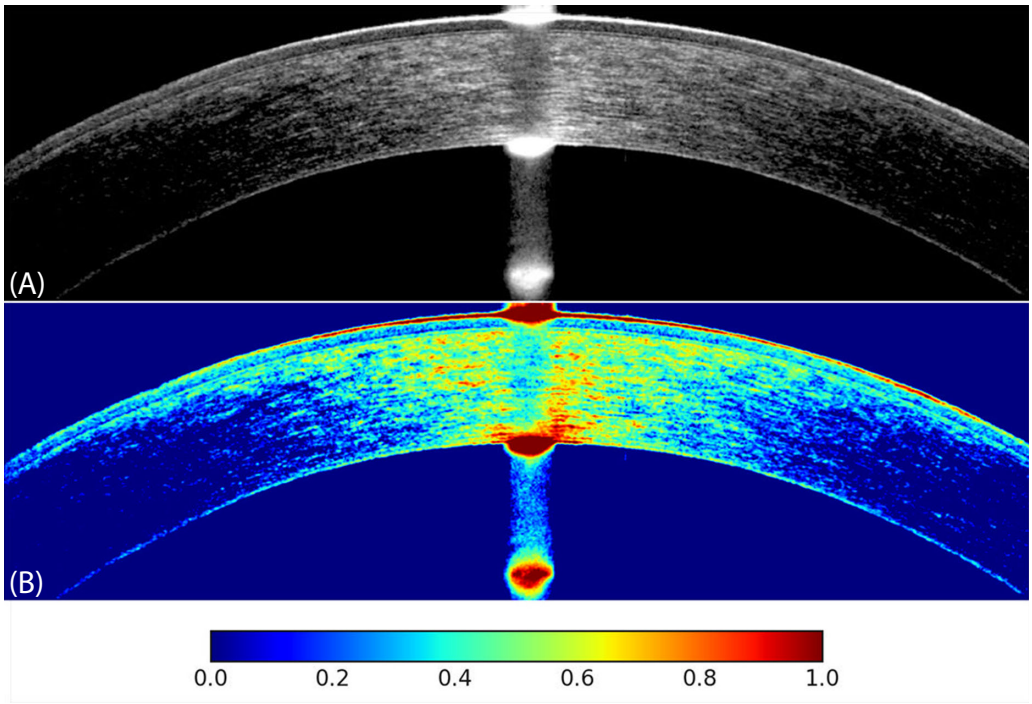

Figure 6. (**A**) 6-mm wide cornea OCT B-scan in log scale with enhanced contrast for improved visualization. The central flare is a mirror artifact excluded from our image analysis. Parallel organized fibrils are visible in the posterior stroma. (**B**) The same OCT B-scan converted to color scale, better illustrating the reflectance. Note the higher reflectance in the posterior stroma, as well as the high reflectance in the epithelium, anterior stroma, and endothelium at higher incidence angles, corroborated by Figure 3.

lamellar organization with collagen fibers arranged parallel to the corneal surface.[2] Moreover, keratocytes, which are transparent except for their nuclei,[2] contribute up to 15% of the stromal volume[21] and are thought to limit backward scattering.[22] Studies have shown increased keratocyte density in the anterior stroma.[23,24]

Wang et al.[25] further elaborated that the gradient of mean corneal densitometry values could be due to a combination of factors, including differences in refractive indices across the cornea, variations in hydration in the axial direction, differences in lamellar structure, and differences in the ratio of keratocytes. Thus corneal reflectance might result from the interplay of these factors. Our observations align with this perspective, suggesting that the structural differences between the anterior and posterior stroma contribute to the variations in reflectance profiles.

To further illustrate these reflectance differences, an OCT B-scan of the cornea is shown in Figure 6. The reflectance profile is non-homogeneous, as expected. The stroma exhibits distinct reflectance patterns, with higher intensity observed in the posterior stroma. At higher incidence angles, reflectance is more pronounced in the epithelium, anterior stroma, and endothelium, likely due to a lower directional component. The posterior stroma shows more organized fibrils, visible in Figure 6A, contributing to a stronger and more directional reflectance. These reflectance differences between the anterior and posterior stroma are consistent with our model.

Previous studies have reported varying results regarding stromal reflectance profiles. Dhubhghaill et al.[26] and Ning et al.,[27] using Scheimpflug imaging, observed higher densitometry values in the anterior corneal layers compared to the middle and posterior layers. In contrast, Wang et al.,[25] using OCT imaging (wavelength = 850 nm), reported that normal corneas exhibited the highest backscatter in the epithelium and posterior stroma, with the anterior stroma showing lower backscatter.

Knighton et al.[6,7] used an ex vivo approach to study retinal nerve fiber layer reflectance, adjusting the camera and light source to observe directional changes. In contrast, we used an in vivo method using OCT, leveraging the natural curvature of the cornea to achieve variation in incidence angles. By assuming homogeneity in corneal properties across similar depths, our approach avoids the need for physical manipulation and allows for a more practical, clinically relevant analysis of reflectance patterns.

Our study extends the work of previous researchers by providing quantitative models that account for the angle of incidence in corneal reflectance, a factor

not explored in earlier studies. Although Scheimpflug imaging has been used to assess corneal densitometry,[26,27] it suffers from poor axial resolution and inability to segment individual corneal layers. OCT provides higher resolution and layer-specific imaging capabilities, which we used to gain detailed insights into the optical behavior of each corneal layer.

Modeling corneal reflectance as a function of incidence angle holds significant clinical potential. Quantitative metrics derived from these models could improve the diagnostic capabilities of OCT by detecting early microstructural changes in the cornea, such as those seen in keratoconus, Fuchs' dystrophy, or corneal scarring.[8,9] Increased reflectance in specific stromal layers may indicate early stromal haze or scarring, allowing for earlier intervention.[28] Importantly, our findings suggest that nonparametric percentile analysis, such as evaluating the 97th percentile reflectance, should be favored over parametric mean-based models for detecting localized scattering events such as opacities, edema, or haze.[25,28,29] This is because parametric mean reflectance models do not account for normal variations in high-intensity scattering events, potentially misclassifying normal high reflectance as opacity, whereas percentile analysis is sensitive to these outliers. Additionally, exploring the relationship between reflectance and directionality patterns and specific corneal diseases could lead to new diagnostic criteria or monitoring tools.

In addition to our modeling, we performed a variance component analysis on the superpixel-level residuals—defined as the percentage deviation between the measured and model-predicted reflectance—to elucidate the sources of variability in our dataset. In the linear domain, the total normalized variance was 0.42 for the epithelium, 0.56 for the stroma, and 0.49 for the endothelium. Notably, the stroma exhibited the highest overall variability, likely reflecting its complex collagen architecture, whereas the epithelium showed relatively consistent reflectance. Further partitioning revealed that in the epithelium, 31.4% of the variance was attributable to between-patient differences, 6.3% to between-eye differences, and 62.3% to within-eye variability. Similar patterns were observed in the stroma and endothelium—with the endothelium displaying the highest between-patient variability (38.8%) and between-eye variability (10.5%)—suggesting that, in addition to local microstructural heterogeneity, inter-individual differences in the endothelium may be driven by factors such as variations in endothelial cell density or other patient-specific factors, possibly including subclinical endothelial dysfunction or age-related changes.

Moreover, both Pearson correlation and two-sample *t*-test analyses revealed no significant associations between patient age or gender and the normalized residual variance in any layer. It is noteworthy that variance estimates computed in the linear domain are higher than those that would be obtained in the logarithmic domain due to dynamic range compression.

Although our study is limited by its retrospective design, its limited sample size, and the exclusive inclusion of normal eyes, it establishes a robust framework for modeling corneal reflectance. Although previous studies have linked corneal densitometry to demographic factors,[26,27] our findings suggest that, when reflectance is quantified on OCT via our approach, such influences are minimal. Importantly, although our cohort was imaged using a single, calibrated OCT system, we believe that—with appropriate calibration and data conversion—the mathematical model presented here can be extended and applied across different OCT devices.

In summary, our work enhances the understanding of corneal optical properties by providing a detailed quantitative model of directional reflectance that accounts for depth incidence angle variability. This model holds significant potential for improving OCT-based diagnostics and lays the groundwork for future investigations into the complex interplay between corneal microstructure and optical behavior.

Acknowledgments

Supported by the National Institutes of Health (Bethesda, MD) (grants no.: R01EY028755, R01EY029023, R21EY034330, and P30EY010572), a research grant and equipment support from Visionix USA (formerly Optovue, Inc.); the Malcolm M. Marquis, MD Endowed Fund for Innovation, and an unrestricted grant from Research to Prevent Blindness (New York, NY) to Casey Eye Institute, Oregon Health & Science University.

Disclosure: **J.F. Assaf**, NeuralVision – FZCO, UAE (S, O); **J. Hong**, Visionix USA (F); **Y. Li**, Visionix USA (F, P); **D. Huang**, Visionix USA (formerly Optovue) (F, P, R), Genentech (P, R), Intalight (F), Canon (F), Cylite (F)

References

1. DelMonte DW, Kim T. Anatomy and physiology of the cornea. *J Cataract Refract Surg*. 2011;37:588–598.

2. Meek KM, Knupp C. Corneal structure and transparency. *Prog Retin Eye Res*. 2015;49:1–16.
3. Huang D, Swanson EA, Lin CP, et al. Optical coherence tomography. *Science*. 1991;254(5035):1178–1181.
4. Ramos JLB, Li Y, Huang D. Clinical and research applications of anterior segment optical coherence tomography–a review. *Clin Exp Ophthalmol*. 2009;37:81–89.
5. Drexler W, Fujimoto JG. State-of-the-art retinal optical coherence tomography. *Prog Retin Eye Res*. 2008;27:45–88.
6. Knighton RW, Huang X, Zhou Q. Microtubule contribution to the reflectance of the retinal nerve fiber layer. *Invest Ophthalmol Vis Sci*. 1998;39:189–193.
7. Knighton RW, Huang XR. Directional and spectral reflectance of the rat retinal nerve fiber layer. *Invest Ophthalmol Vis Sci*. 1999;40:639–647.
8. Rabinowitz YS. Keratoconus. *Surv Ophthalmol*. 1998;42:297–319.
9. Weiss JS, Møller HU, Lisch W, et al. The IC3D Classification of the Corneal Dystrophies. *Cornea*. 2008;27(Suppl 2):S1–S83.
10. Hagen-Eggert M, Koch P, Hüttmann G. Analysis of the signal fall-off in spectral domain optical coherence tomography systems. In: *Optical Coherence Tomography and Coherence Domain Optical Methods in Biomedicine XVI*. Bellingham, WA: SPIE; 2012; 8213:161–167.
11. Yu H, Gao J, Li A. Probability-based nonlocal means filter for speckle noise suppression in optical coherence tomography images. *Opt Lett*. 2016;41:994–997.
12. Hulst HC, van de Hulst HC. *Light Scattering by Small Particles*. North Chelmsford, MA: Courier Corporation; 1981.
13. Bohren CF, Huffman DR. *Absorption and Scattering of Light by Small Particles*. Hoboken, NJ: John Wiley & Sons; 2008.
14. Ruberti JW, Roy AS, Roberts CJ. Corneal biomechanics and biomaterials. *Annu Rev Biomed Eng*. 2011;13:269–295.
15. Komai Y, Ushiki T. The three-dimensional organization of collagen fibrils in the human cornea and sclera. *Invest Ophthalmol Vis Sci*. 1991;32:2244–2258.
16. Patel DV, McGhee CNJ. Mapping of the normal human corneal sub-basal nerve plexus by in vivo laser scanning confocal microscopy. *Invest Ophthalmol Vis Sci*. 2005;46:4485–4488.
17. Beuerman RW, Pedroza L. Ultrastructure of the human cornea. *Microsc Res Tech*. 1996;33:320–335.
18. Bergmanson JPG, Horne J, Doughty MJ, Garcia M, Gondo M. Assessment of the number of lamellae in the central region of the normal human corneal stroma at the resolution of the transmission electron microscope. *Eye Contact Lens*. 2005;31:281.
19. Abahussin M, Hayes S, Knox Cartwright NE, et al. 3D collagen orientation study of the human cornea using X-ray diffraction and femtosecond laser technology. *Invest Ophthalmol Vis Sci*. 2009;50:5159–5164.
20. Radner W, Zehetmayer M, Aufreiter R, Mallinger R. Interlacing and cross-angle distribution of collagen lamellae in the human cornea. *Cornea*. 1998;17:537.
21. Huang Y, Meek KM. Swelling studies on the cornea and sclera: the effects of pH and ionic strength. *Biophys J*. 1999;77:1655–1665.
22. Piatigorsky J. Gene sharing in lens and cornea: facts and implications. *Prog Retin Eye Res*. 1998;17:145–174.
23. Møller-Pedersen T, Ehlers N. A three-dimensional study of the human corneal keratocyte density. *Curr Eye Res*. 1995;14:459–464.
24. Patel SV, McLaren JW, Hodge DO, Bourne WM. Normal human keratocyte density and corneal thickness measurement by using confocal microscopy in vivo. *Invest Ophthalmol Vis Sci*. 2001;42:333–339.
25. Wang J, Simpson TL, Fonn D. Objective measurements of corneal light-backscatter during corneal swelling, by optical coherence tomography. *Invest Ophthalmol Vis Sci*. 2004;45:3493–3498.
26. Ní Dhubhghaill S, Rozema JJ, Jongenelen S, Ruiz Hidalgo I, Zakaria N, Tassignon MJ. Normative values for corneal densitometry analysis by Scheimpflug optical assessment. *Invest Ophthalmol Vis Sci*. 2014;55:162–168.
27. Ning J, Sun S, Zhang Q, et al. Corneal densitometry in Chinese adults with healthy corneas: associations with sex, age, ocular metrics, and optical characteristics. *BMC Ophthalmol*. 2024;24:230.
28. Dhaini AR, Chokr M, El-Oud SM, Fattah MA, Awwad S. Automated detection and measurement of corneal haze and demarcation line in spectral-domain optical coherence tomography images. *IEEE Access*. 2018;6:3977–3991.
29. Rose JS, Eldrina J, Joshua A, et al. Objective quantification of corneal haziness using anterior segment optical coherence tomography. *J Curr Ophthalmol*. 2018;30:54–57.